Reprinted from JOURNAL OF APPLIED METEOROLOGY, Vol. 32, No. 4, April 1993
American Meteorological Society

Effect of Amazon Smoke on Cloud Microphysics and Albedo—Analysis from Satellite Imagery

YORAM J. KAUFMAN

NASA/Goddard Space Flight Center, Greenbelt, Maryland

TERUYUKI NAKAJIMA

Center for Climate System Research, University of Tokyo, Hongo, Bunyo-ku, Tokyo, Japan

(Manuscript received 6 January 1992, in final form 6 July 1992)

ABSTRACT

NOAA Advanced Very High Resolution Radiometer images taken over the Brazilian Amazon Basin during the biomass burning season of 1987 are used to study the effect of smoke aerosol particles on the properties of low cumulus and stratocumulus clouds. The reflectance at a wavelength of 0.64 μm and the drop size, derived from the cloud reflectance at 3.75 μm, are studied for tens of thousands of clouds. The opacity of the smoke layer adjacent to each cloud is also monitored simultaneously. Though from satellite data it is impossible to derive all the parameters that influence cloud properties and smoke–cloud interaction (e.g., detailed aerosol particles size distribution and chemistry, liquid water content, etc.); satellite data can be used to generate large-scale statistics of the properties of clouds and surrounding aerosol (e.g., smoke optical thickness, cloud-drop size, and cloud reflection of solar radiation) from which the interaction of aerosol with clouds can be surmised. In order to minimize the effect of variations in the precipitable water vapor and in other smoke and cloud properties, biomass burning in the tropics is chosen as the study topic, and the results are averaged for numerous clouds with the same ambient smoke optical thickness.

It is shown in this study that the presence of dense smoke (an increase in the optical thickness from 0.1 to 2.0) can reduce the remotely sensed drop size of continental cloud drops from 15 to 9 μm. Due to both the high initial reflectance of clouds in the visible part of the spectrum and the presence of graphitic carbon, the average cloud reflectance at 0.64 μm is reduced from 0.71 to 0.68 for an increase in smoke optical thickness from 0.1 to 2.0. The measurements are compared to results from other years, and it is found that, as predicted, high concentration of aerosol particles causes a decrease in the cloud-drop size and that smoke darkens the bright Amazonian clouds. Comparison with theoretical computations based on Twomey's model show that by using the measured reduction in the cloud-drop size due to the presence of smoke it is possible to explain the reduction in the cloud reflectance at 0.64 μm for smoke imagery index of -0.02 to -0.03.

Smoke particles are hygroscopic and have a similar size distribution to maritime and anthropogenic sulfuric aerosol particles. Therefore, these results may also be representative of the interaction of sulfuric particles with clouds.

1. Introduction

Biomass burning produces large quantities of smoke that may have a large effect on the atmosphere and climate (Crutzen and Andreae 1990; Penner et al. 1992). Smoke particles scatter sunlight and serve as cloud condensation nuclei (CCN) in a similar way to sulfate particles (Warner and Twomey 1967; Radke 1989; Hobbs and Radke 1969; Holben et al. 1991; Kaufman et al. 1992). Though the extent of their effect is not well studied, it is estimated to be similar within an order of magnitude to the sulfate effect (Radke et al. 1989; Penner et al. 1991). The effect of smoke on clouds may be simpler than the effect of sulfates on clouds since most submicron smoke particles are generated close to the fire from condensation of organic gases, while SO_2 is converted to sulfate particles in dry air and inside clouds during several days. Therefore, smoke particles are best suitable for the detection of the effect of anthropogenic aerosol on clouds, and the effect of smoke on clouds can be considered as an experimental test of the effect of aerosol particles on clouds in general. Empirical observations of the dependence of cloud-droplet concentration on airmass origin and aerosol source were first reported by Squires (1956). Squires and Twomey (1960) demonstrated that maritime and continental clouds showed considerable difference in their droplet population and in the consequent rainfall. Squires (1966) recognized that at least in some areas anthropogenic sources can be as effective as natural sources in producing CCN particles. Later measurements also showed that an increase in the CCN concentration usually causes an increase in

Corresponding author address: Yoram J. Kaufman, NASA/Goddard Space Flight Center, Code 913, Greenbelt, MD 20771.

the cloud-droplet concentration (Twomey and Warner 1967; Leaitch et al. 1986), resulting in a larger cloud albedo (Twomey et al. 1984; Coakley et al. 1987; Radke et al. 1989). There are also indications that the increased CCN concentration, at least in the case of stratiform clouds, increases the cloud lifetime by suppressing drizzle (Albrecht 1989). Warner (1968) has found that the high CCN concentration from smoke generated by sugarcane fires in Australia reduces precipitation, while CCN from industrial sources emitted to an atmosphere with small initial CCN concentration increase the probability of precipitation (Hobbs et al. 1970). Industrially induced CCN concentration quickly converts water vapor into large cloud drops and initiates precipitation.

Biomass burning, as well as fossil fuel consumption, has two competing effects on the climate system. The first is a direct warming associated with CO_2 emission (Manabe and Wetherald 1980; Hansen et al. 1984). The second is a cooling caused by SO_2-derived aerosol, which may either contribute to the cooling directly by backscattering solar radiation (Coakley et al. 1983; Charlson et al. 1991) or indirectly by increasing the concentration of CCN that in turn may lead to smaller and more numerous cloud droplets and higher cloud albedos and thus indirectly contribute to additional reflectance of solar radiation to space. The sulfur compounds increase the CCN concentration from values as low as 30–50 cm^{-3} in remote oceanic regions where anthropogenic SO_2 is minimal (Twomey 1959; Twomey and Wojciechowski 1969; Radke 1989) to 1000–4000 cm^{-3} in regions contaminated by industrial pollution (Braham 1974) or by smoke from fires (Warner and Twomey 1967; Radke 1989).

At the present emission levels from industrial or biomass burning sources, aerosol cooling, both directly through reflection of sunlight to space and indirectly thorough the aerosol effect on cloud properties, has the potential to offset the CO_2-induced warming (Twomey et al. 1984; Kaufman et al. 1991; Charlson et al. 1991; Wigley 1991; Penner et al. 1992). The prediction of the effect of SO_2-derived aerosol is difficult due to the complex interactions of SO_2 with atmospheric water vapor, aerosol, and clouds (Hansen and Lacis 1990; Charlson et al. 1990; Twomey 1991). In fact, the uncertainty in the effect of anthropogenic aerosol on clouds and climate is considered as "*the greatest uncertainty in climate forcing*" (Hansen and Lacis 1990). One of the major uncertainties in the study of the indirect SO_2 climatic effect is in the estimation of the relationship between the CCN concentration and the concentration of the anthropogenic aerosol (Wigley 1989; Charlson et al. 1990) and the emission of sulfuric compounds (Twomey 1991). The uncertainty results from the short and variable lifetime of atmospheric sulfur compounds, a nonhomogeneous distribution of sources, complex interaction with clouds, and a variable vertical distribution of concentration. Leaitch et al. (1986) found that cloud-drop concentration (CDC) and CCN concentration saturates with respect to sulfate concentration around 1000–1500 cm^{-3}, in contrast to the higher saturation levels suggested by Twomey (1977) and to the large CCN and CDC concentrations of up to 3000 cm^{-3} measured by Braham (1974). Based on the theoretical analysis by Baker and Charlson (1990), it can be concluded that the relationship between the CCN concentration and the aerosol concentration may be nonlinear, resulting in two main possible levels of CCN concentrations rather than a continuous function.

To reduce the uncertainties in the relationship between the anthropogenic emissions and cloud albedo, two possible paths can be taken.

1) Aircraft measurements can be made relating SO_2 in the atmosphere to the formation of CCN and cloud drops (Radke 1989; Rawlins and Foot 1990; Nakajima et al. 1991). Aircraft measurements can include also many other relevant parameters, for example, liquid water content and chemistry (Leaitch et al. 1986, 1992) and aerosol particle concentration and size distribution (Radke et al. 1991).

2) A statistical analysis can be done of the relationship between numerous individual cloud characteristics and the characteristics of the aerosol surrounding these clouds.

In this paper, we shall undertake the second approach, namely analysis of satellite data of large regions covered by broken clouds and varying amounts of haze (smoke particles). Cloud characteristics are affected not only by the concentration of CCN, but also by other environmental factors, such as weather patterns and cloud type, strength of the convection process, availability of water vapor, and illumination directions. Therefore, it is imperative for this task to use a remote-sensing technique that will resolve the effect of CCN's from the other environmental effects. This is accomplished by choosing the dry season in the Amazon Basin where these effects are minimal and by averaging the remote-sensing results on a large number of clouds.

In section 2, smoke and clouds in the Amazon Basin are described. The remote-sensing procedure is described in section 3. Results are reported in section 4 and compared with a theoretical model based on Twomey's theory in section 5. Section 6 concludes the paper.

2. Smoke and clouds in the Amazon Basin

Deforestation fires in the Amazon Basin (Tucker et al. 1984; Malingreau and Tucker 1988; Setzer and Pereira 1991) generate smoke of variable density across millions of square kilometers during the dry season (June–October; Kaufman et al. 1990b, 1992). In general, there are many complex meteorological conditions that determine cloud development and albedo, for ex-

ample, absorption by graphitic carbon that can accompany the haze, precipitable water vapor, atmospheric stability that affects the strength of the convection, cloud development, and cloud type. It is difficult to isolate the effect of aerosols under such conditions. In the Amazon dry season, however, the cloud optical properties are weakly dependent on variations in the meteorological conditions, unlike midlatitude regions. The occurrence of smoke is almost independent of meteorological conditions (except rain, wind speed, and direction); thus, for example, during the burning season we do not expect a strong correlation between precipitable water vapor and the presence of smoke. Measurements during a short period in the dry season in Brazil revealed that in contrast to the strong spatial and daily variation in the aerosol concentration, the water vapor profile is very stable (2–3 cm of precipitable water vapor; Kaufman et al. 1992). The Amazon Basin is also characterized by a uniform surface cover of forest, with low uniform reflectance in the visible and mid IR parts of the spectrum and high reflection in the near IR. These characteristics enable easier (and more accurate) determination of smoke optical thickness, single-scattering albedo, and cloud characteristics.

3. Remote sensing of aerosol interaction with clouds

The application of satellite data to remote sensing of smoke and clouds is based on measurements of aerosol properties acquired from an aircraft in a field experiment in 1989 in Brazil (Holben et al. 1991; Kaufman et al. 1992) and on a large dataset of the afternoon NOAA Advanced Very High Resolution Radiometer (AVHRR) satellite imagery with 1-km resolution that was archived at NASA/Goddard Space Flight Center (Tucker, personal communication). AVHRR data from 1981, 1984, 1987, and simultaneously with the field experiment in 1989 are used.

The AVHRR dataset and the measured smoke properties, described by Kaufman et al. (1990b, 1992), are used in this study. Three AVHRR channels are used. The red channel, 0.64 μm, the midinfrared, 3.75 μm, and the infrared, 11 μm. The area of investigation is selected in a region that during the beginning of the dry season (first half of June 1987, before significant biomass burning takes place) shows low surface reflectance (surface plus atmospheric reflectance of less than 0.08 or surface reflectance less than 0.04) in the AVHRR 0.64-μm channel. The chosen region included most of the rectangular area from 48° to 64°W and 2° to 19°S, roughly 3 000 000 km^2. The same region was used in the analysis of all the images processed in this study.

To further reduce the effect of meteorological variables, a large statistical sample is taken of cloud properties and of the concentration of aerosol particles in the vertical column adjacent to each individual cloud. To avoid the effect of angular dependence of the cloud reflectance, aerosol scattering, and surface properties, only data for nadir view ±20° are included. The following characteristics of individual clouds are analyzed from the AVHRR measurements (based on Arking and Childs 1985; Nakajima and King 1990; Nakajima et al. 1991).

- Cloud reflectance and optical thickness using the 0.64-μm channel. The analysis is performed on pixels of the cloud that are not located on the perimeter of the cloud in order to reduce errors from partial cloud cover within pixels and to reduce the effect of cloud edges.
- Cloud-drop size derived from the average cloud reflectance (excluding the cloud perimeter) in the 3.75-μm channel.
- Cloud size and number of pixels on its perimeter.
- Cloud-top temperature using the IR (11-μm) channel. Cloud-top temperature, area, and length of the perimeter are related to the cloud type and cloud development and can indicate the probability of a given cloud to interact with the smoke layer.

Note that there is a consistent overestimation, by 25%–50%, of the cloud-drop size derived by remote-sensing techniques relative to in situ measurements (Twomey and Cocks 1982, 1989; Rawlins and Foot 1990; Nakajima et al. 1991). The vertical inhomogeneity of drop size cannot explain this difference, with the latest explanation of the difference attributed to anomalous absorption by water vapor (Stephens and Tsay 1990). Therefore, the analysis in this paper is used to detect the variation of drop size as a function of the aerosol loading adjacent to large clouds rather than to measure the absolute cloud-drop size.

Well-developed clouds (cloud reflectance $\rho_c > 0.4$) are the focus here. Radiative transfer computations show that for these clouds, the cloud optical thickness and drop size can be derived directly from reflectance measurements in the visible and mid-IR (2–4 μm) window parts of the spectrum since these reflectances are almost orthogonal functions (Nakajima and King 1990; Fig. 1). Note that the drop size, detected from the AVHRR 3.75-μm channel, represents the conditions of only the upper layer of the cloud, due to the strong absorption of radiation in the mid-IR by the cloud drops (Nakajima and King 1990). For example, for drop size of 8 μm, there is no evident sensitivity to the cloud optical thickness, τ_c, for $\tau_c > 6.0$ (see Fig. 1). Thus, for a thick cloud ($\tau_c > 6.0$), the reflectance is not sensitive to the cloud properties in the part of the cloud that is below the top layer with $\Delta\tau_c > 6.0$. For the clouds analyzed in this study, the average cloud optical thickness is 50, therefore, $\Delta\tau_c = 6.0$ corresponds to top one-eighth of the cloud optical thickness. Note that this cloud portion is the most important in radiative processes since it determines most of the reflection of solar radiation to space.

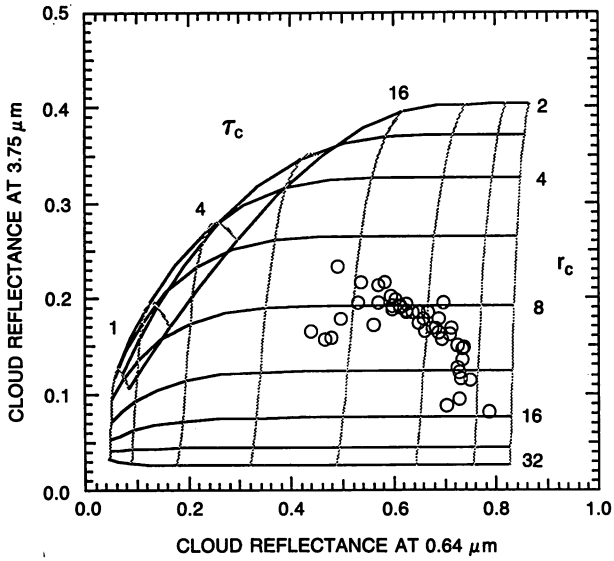

FIG. 1. Contour lines of equal cloud optical thickness (τ_c—gray lines) and equal average drop radius (r_c—black lines) in coordinates of the cloud reflectance in the 0.64-μm channel and the 3.75-μm channel. Except for small drop size or small cloud optical thickness, the lines are almost orthogonal, indicating that the optical thickness and the drop size can be detected from these two AVHRR channels. The AVHRR data for clouds in Brazil, averaged for equal steps of the cloud-free radiance (indicating the smoke optical thickness) are also plotted (O). The theoretical data and the measurements are averaged for the two azimuths (30° and 150°) for θ_0 = 60° and average view direction of 10°.

In order to reduce the variability in the cloud optical thickness and drop size associated with cloud type and development, we concentrate on remote sensing of low cumulus and stratocumulus clouds, which are no more than a few tens of kilometers in diameter. Low clouds also have higher probability for interacting with the smoke aerosol layer. Thus, the properties of an ensemble of clouds can be expected to be affected mainly by the concentration of CCN and graphitic carbon, which are influenced by fire and anthropogenic emissions. The effect of variation in meteorological conditions is expected to be canceled in the averaging process.

The remote-sensing procedure includes the following steps.

- The cloudy pixels are identified. Since our interest lies only in low dense clouds, and the surface in the selected area is uniform and dark in the 0.64-μm channel, cloudy pixels are identified as pixels with reflectance $\rho_{0.64} > 0.4$.
- Clouds are identified. The cloudy pixels are grouped into individual clouds based on their spatial locations.

For each cloud the following analysis is performed.

- The average reflectances of the cloud in the 0.64-μm and 3.75-μm channels and the average temperature from the 11-μm channel are stored. The information is averaged on all the cloudy pixels that are not on the perimeter. In the mid-IR (3.75 μm), in addition to the reflection of sunlight, there is also contribution from thermal emission. The cloud reflectance in the mid-IR was computed assuming that the emissivity of clouds in the IR (11 μm) is equal to 1.0, that the transmission through a cloud in the 3.75-μm channel is zero, and that the sum of the surface directional reflectance and the emissivity in this channel is also 1. The transmission at 3.75 μm can be neglected for clouds with optical thickness above 10 (King and Harshvardhan 1986). Therefore, the relationship between the total radiance at 3.75 μm ($L_{3.7}$) and at 11-μm (L_{11}) channels to the reflectance at 3.75 μm ($\rho_{3.7}$) is

$$L_{3.7} = t^0_{3.7}\left(\frac{F_0\mu_0}{\pi}\right)\rho_{3.7} + t'_{3.7}B_{3.7}(T)(1-\rho_{3.7}) \quad (1)$$

$$L_{11} = t'_{11}B_{11}(T), \quad (2)$$

where $t^0_{3.7}$ is the total downward and then upward transmission above the cloud of sunlight at the 3.75-μm channel; $t'_{3.7}$ and t'_{11} are the upward transmissions above the cloud at the 3.7-μm and 11-μm channels, respectively; F_0 is the extraterrestrial solar flux in the 3.75-μm channel; μ_0 is the cosine of the solar zenith angle; and $B_i(T)$ is the Plank function for temperature T and wavelength i. From (1) and (2), the relationship between the cloud reflectance $\rho_{3.7}$ and the measured radiance at 3.75 μm ($L_{3.7}$) and 11 μm (L_{11}) can be derived:

$$\rho_{3.7} = \frac{L_{3.7} - t'_{3.7}B_{3.7}(T)}{(t^0_{3.7}F_0\mu_0/\pi) - [t'_{3.7}B_{3.7}(T)]}, \quad \text{where}$$

$$T = \frac{1}{B_{11}}\frac{L_{11}}{t'_{11}}. \quad (3)$$

The transmission functions $t^0_{3.7}$, $t'_{3.7}$, and t'_{11} depend on the precipitable water above the cloud.

- The brightest pixel of each cloud (in the 0.64-μm channel) is identified and its reflectance in the 0.64-μm and 3.75-μm channel, along with its temperature, are recorded. The difference between the temperature of this pixel and the average temperature of the cloud are indicators of the cloud-top roughness. The brightest pixel is also less sensitive to processes that occur in the cloud edge, and therefore better represents the cloud interior.
- The area of the cloud and the number of pixels on its perimeter are stored.
- The minimal apparent reflectance of the cloud-free area (ρ^*_f) at 0.64 μm, adjacent to the cloud on its sunny side, is stored. The reflectance of the cloud free area, ρ^*_f, is a result of surface reflectance and scattering and absorption by smoke particles and atmospheric gases. It is defined as the upward radiance, L, normalized to reflectance units, $\pi L/F'_0\mu_0$, where F'_0 is the extraterrestrial flux in the 0.64-μm channel. The value of ρ^*_f is found as the minimal reflectance in a scan line

of 10 pixels adjacent to the cloud on its west side (to avoid shadows). The average of these values, ρ^*_{fa}, for all the westerly scan lines that correspond to a given cloud and the minimum, ρ^*_{fm}, are stored. The difference between them, $\rho^*_{fa} - \rho^*_{fm}$, is used instead of the variance in the one-dimensional clustering technique of Coakley and Bretherton (1982) as a possible indication of cloud contamination of the supposedly cloud-free area; clouds for which $\rho^*_{fa} - \rho^*_{fm} > 0.03$ are not included in the analysis. The average cloud-free reflectance ρ^*_f is inverted into the smoke aerosol optical thickness τ_a using a smoke aerosol model (Holben et al. 1990; Kaufman et al. 1992) and an assumed value of the forest reflectance of 0.02 (Kaufman and Sendra 1988). Here τ_a is a measure of the aerosol mass loading (Fraser et al. 1984) and is used here as a measure of the aerosol particles concentration. This issue is discussed in the theoretical section.

The measured cloud reflectance at the 3.75-μm channel ($\rho_{3.7}$) is used to derive the cloud-drop size r_c using a theoretical relationship between $\rho_{3.7}$ and r_c, as shown in Fig. 1 and discussed in the theoretical section. The transmission in the 11-μm channel, t'_{11}, reduces the apparent radiative temperature of the cloud, while the transmission in the 3.75-μm channel, $t'_{3.7}$, reduces the transmission of the emitted radiation in the 3.75-μm channel. Therefore, these two transmissions tend to balance each other in (3). Since the amount of water vapor above the clouds is uncertain, the effect of water vapor is simplified by assuming that both transmissions are $t'_{3.7} = t'_{11} = 1$ and that the transmission of the reflected sunlight is $t^0_{3.7} = 0.75$ (corresponding to 0.7 cm of water above the cloud). A sensitivity study to a range of values in the transmission factors shows that the resultant uncertainty in the drop radius r_c is $\Delta r_c = \pm 0.01$ μm.

4. Measurements

a. Characteristics of the cloud field

The general characteristics of the cloud properties as a function of the cloud-top temperature are shown in Fig. 2. This figure is used here to show the repeatability of the cloud properties both from year to year and from one dry period interval to another. They are also used to derive the range of the cloud characteristics in which the effect of smoke can be observed. Figure 2 shows the number of clouds per kelvin of cloud-top temperature, the cloud size, and the cloud reflectance in the 0.64-μm and 3.75-μm channels as a function of the cloud-top temperature. Although in this paper we concentrate on the analysis of images from 1987 (central column in Fig. 2), a sample statistics for 1981, 1984, and 1989 are also shown (left column). The average properties of the clouds for these four years are shown in the right column. The data for 1987 (central column) were divided into four groups corresponding to different periods in the dry season: in the main set (set A), nine images represent the whole biomass burning season (7 July–18 September); in the control set (set B), the four images are from the beginning of the dry season before major burning takes place (30 June–6 July); in set C, seven images from the beginning of the burning period are shown (15 July–30 July); and set D, six images are from the end of the dry season (7 August–2 September).

A comparison between a given cloud property in the right column and that in the other two columns can show how repetitive the properties are from year to year and from one part of the dry season to another.

- Number of clouds peaks around 280 K and decreases exponentially (linear in the figure) with the reduction of the cloud-top temperature. This characteristic is repetitive from year to year and across the dry season of 1987.
- Cloud size increases exponentially (linear in the figure) with the reduction of the cloud-top temperature. The results are again very similar for all periods of time.
- Cloud reflectance in the 0.64-μm channel does not show any substantial difference among the four periods in 1987, even though the amount of smoke is varying from the beginning to the end of the dry season. The cloud reflectance in 1984 for the temperature range 260 K > T > 290 K is larger than in other years.
- Cloud reflectance in the 3.75-μm channel for 1987 shows dependence on the date of a given dataset. For the last dataset, taken in the dry season, with maximal smoke emission from biomass burning, the cloud reflectance is maximal indicating a minimum in the drop size. This is especially evident for the cloud-top temperature range of 290 K > T > 270 K. The reflectance for 1984 is also much higher than for the other years, indicating smaller drops. The correlation between the high reflectance in the 0.64-μm and 3.75-μm channels for 1984 suggests the possibility of strong influence of smoke. Note that the higher reflectance of the 3.75-μm channel in 1984 and in set D of 1987, shown for 290 K > T > 270 K, reappears for temperature range around 260 K (approximately 7-km altitude) for both cases. This indicates the existance of additional smoke layers probably due to pumping of smoke by strong convection activity in agreement with aircraft observations (Andreae et al. 1988; Kaufman et al. 1992).

This analysis shows some of the characteristics of clouds in the Amazon during the dry season as a function of the cloud-top temperature and the possible effects of smoke on these properties. The latter aspect is analyzed in detail in the next sections.

b. Threshold for cloud-top temperature

In order to choose the appropriate threshold for the cloud-top temperature for optimum observation of the interaction of clouds with the smoke layer, scatterdiagrams between the cloud reflectance in "high smoke

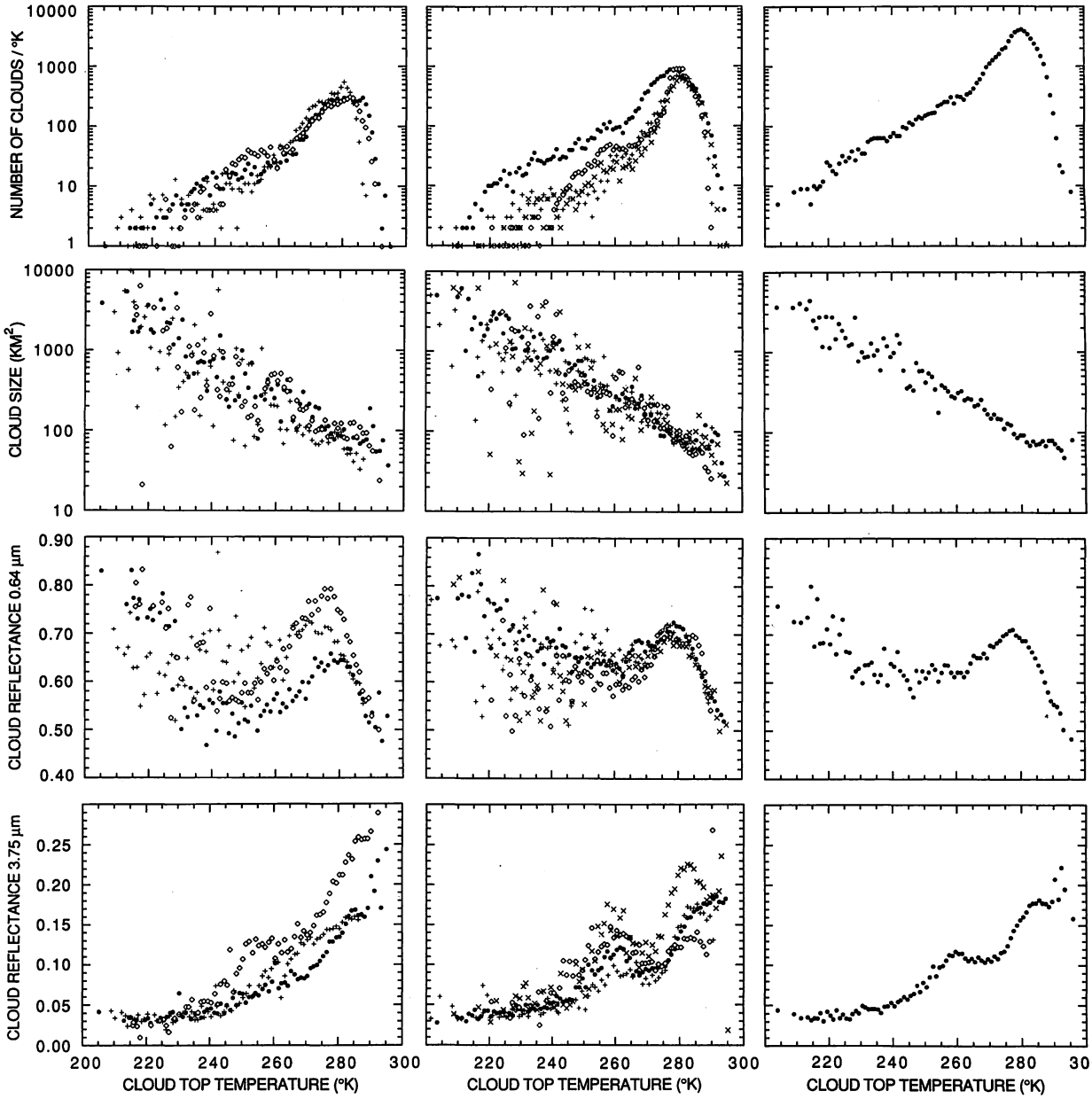

FIG. 2. Statistics of cloud properties as a function of cloud-top temperature. Left column: September–October 1981—(+); August–September 1984—(◇); and September 1989—(O). Middle column: 1987. Right column: average of all the datasets (except for the cloud number that is the sum of all the clouds per kelvin that are used in the analysis). The data for 1987 were divided into four subsets corresponding to different periods of the dry season. Main dataset A (+)—nine images from the whole dry season (7 July–18 September); control set B (◇)—four images from the beginning of the dry season before major burning takes place (30 June–6 July); set C (O)—seven images from the beginning of the burning period (15 July–30 July); and set D (×)—six images for the end of the burning period (7 August–2 September).

concentration" and "low smoke concentration" for the 3.75-μm and 0.64-μm channels are plotted in Fig. 3 and summarized in Table 1. Clouds are separated into two groups based on the density of smoke around them. Clouds in the "high smoke concentration" environment were defined for smoke optical thickness at 0.64 μm, $\tau_a \geqslant 0.4$, and clouds in a "low smoke concentration" environment were defined for $\tau_a < 0.4$. Note that $\tau_a = 0.4$ is about twice the average continental aerosol optical thickness, which over North America is associated with substantial anthropogenic pollution (Peterson et al. 1981; Issac et al. 1986). Therefore, strong anthropogenic effects on clouds are expected already for much smaller aerosol optical thickness (Leaitch et al. 1986, 1992) and will affect also the "low smoke concentration" group. Detailed analysis of the cloud

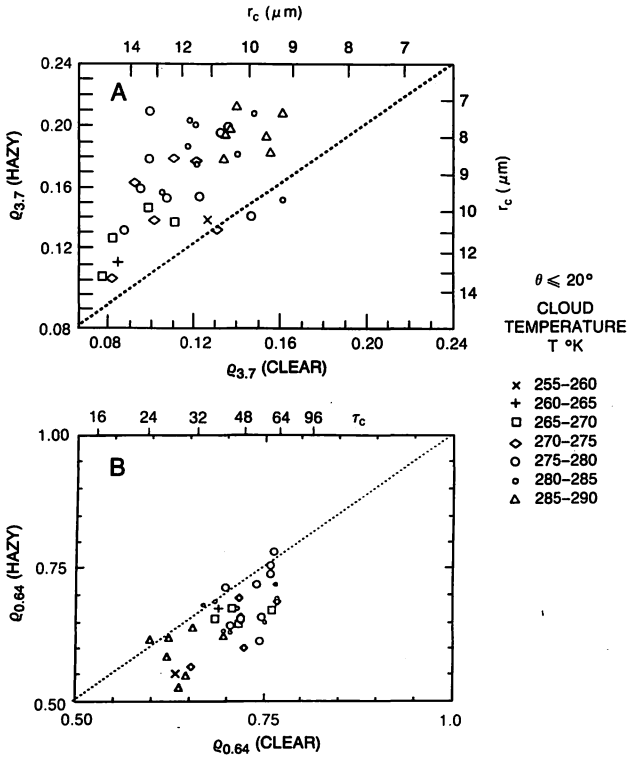

FIG. 3. Scatter diagrams between cloud reflectance in the "high smoke concentration" and the "low smoke concentration" days for the 3.75-μm (top figure) and the 0.64-μm (bottom figure) channels. Clouds for "high" smoke concentration were defined for smoke optical thickness larger than 0.4, and clouds for "low" smoke concentration were defined for optical thickness less than 0.4. The data are for 1987 set A for $\theta \leqslant 20°$. Each point represents an average, for a given day, of the cloud reflectance for all clouds that have cloud-top temperature in a 5° range as indicated in each figure. A value was plotted only if at least 50 clouds were used in the averaging.

properties as a function of the smoke concentration is given in section 4c.

Only images from the 1987 main dataset (A) with view zenith angle of $\theta \leqslant 20°$ were used in Fig. 3. Each point represents an average, for a given day, of the cloud reflectance for all clouds that belong to a given group and that have cloud-top temperature in a 5° range as indicated in the figure. Overall, the smoke increases the reflectance in the mid-IR (or decreases the average drop size) and decreases the reflectance in the visible part of the spectrum. The effect on the drop size is maximal for cloud-top temperature between 275 and 285 K (see Table 1). It is smaller on both sides of this temperature range. This temperature dependence can be also observed to a smaller extent from the data in Fig. 2. As a result, the effect of smoke particles on clouds were analyzed only for those with cloud-top temperatures warmer than 270 K. For a surface temperature of approximately 300 K, this corresponds to a cloud-top height of about 6 km. In Brazil, smoke layers were detected from aircraft observations up to the 4-km altitude (Crutzen et al. 1985; Andreae et al. 1988; Kaufman et al. 1992). The strong convective activity in tropical clouds can pump the smoke to higher altitudes, as indicated from the aerial photograph shown in Fig. 4 and in the effect of smoke on clouds even for clouds with cloud-top temperature less than 270 K (Figs. 2 and 3 and Table 1).

c. *Effect of smoke on clouds for the 1987 biomass burning season*

In Figs. 2 and 3, the effect of smoke particles on the cloud reflectivity in the visible and mid-IR parts of the spectrum and the corresponding cloud-drop size were discussed. In the case of Fig. 2, the presence of smoke differs for the different periods of the dry season. In Fig. 3, clouds were classified into two parts based on the concentration of smoke surrounding each individual cloud. Once the threshold of cloud-top temperature was applied to the dataset, it is possible to measure the effect of smoke on clouds as a function of the optical thickness of the smoke adjacent to each individual cloud, averaging the results on all clouds that have

TABLE 1. The effect of smoke on the cloud-drop size. Average results are given for "low smoke concentration" (smoke optical thickness, $\tau_a < 0.4$) and for "high smoke concentration" ($\tau_a \geqslant 0.4$). The percentage decrease from the "low" to the "high" smoke concentration is also shown. The standard deviations are between the average results for nine images, each one containing at least 50 clouds that belong to a given category.

	Cloud-drop radius (μm)				
	$\tau_a < 0.4$		$\tau_a \geqslant 0.4$		
Temperature (K)	Average	Standard deviation	Average	Standard deviation	Percentage decrease
255–260	12.2		11.5		6
260–265	16.0		13.5		15
265–270	15.2	1.7	12.3	1.5	19
270–275	13.8	1.6	11.2	1.9	19
275–280	13.2	1.7	10.0	1.3	24
280–285	12.1	1.2	9.2	0.6	24
285–290	11.0	0.6	8.9	0.4	20

FIG. 4. Photographs of the smoke interaction with clouds during the biomass burning season in the Amazon Basin. The lower photograph show the source of the smoke on the ground, transport through the condensation level, and the formation of a cloud. The upper picture shows the effect of a strong cumulus cloud in transferring the smoke to higher altitudes when the cloud top stratifies. Note that there is a part of blue sky between the lower and upper smoke layers.

cloud-top temperature warmer than the given threshold (270 K). The results of this analysis are shown in Figs. 5–7. The analysis is based on an underlying assumption that the smoke concentration adjacent to the cloud is representative of the smoke concentration under and in the cloud base. Since most of the smoke is in the boundary layer and the low clouds are formed mainly on top of the boundary layer, (see Fig. 4), this assumption is reasonable. Strong, flaming fires do generate layers of smoke that can be found above the boundary layer.

The statistical information on clouds, shown in Fig. 5, is used later in Figs. 6 and 7 to detect the smoke effect. The cloud number distribution is plotted as a function of ρ_f^* for active biomass burning (7 July–18 September; Fig. 5a) and before active biomass burning started (30 June–6 July; Fig. 5b). The same region was analyzed in both datasets. Smoke during the active biomass burning increased the width of the distribution. The residual width of the distribution in Fig. 5b may result from a combination of variation in the surface reflectance, variation in the concentration of the non-smoke aerosol, contamination from partially clouded pixels, and some early biomass burning.

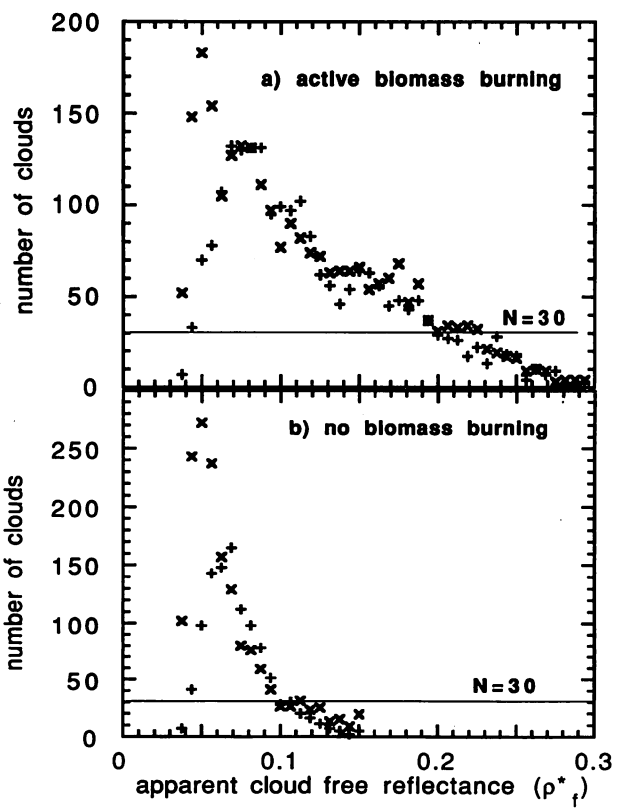

FIG. 5. Number distribution of clouds used in the analysis of the cloud properties in Figs. 6 and 7. The number of clouds used in the averaging for each plotted value is shown as a function of the cloud-free reflectance ρ_f^* at 0.64 μm: (a) for active biomass burning and smoke and (b) for a period preceding extensive biomass burning.

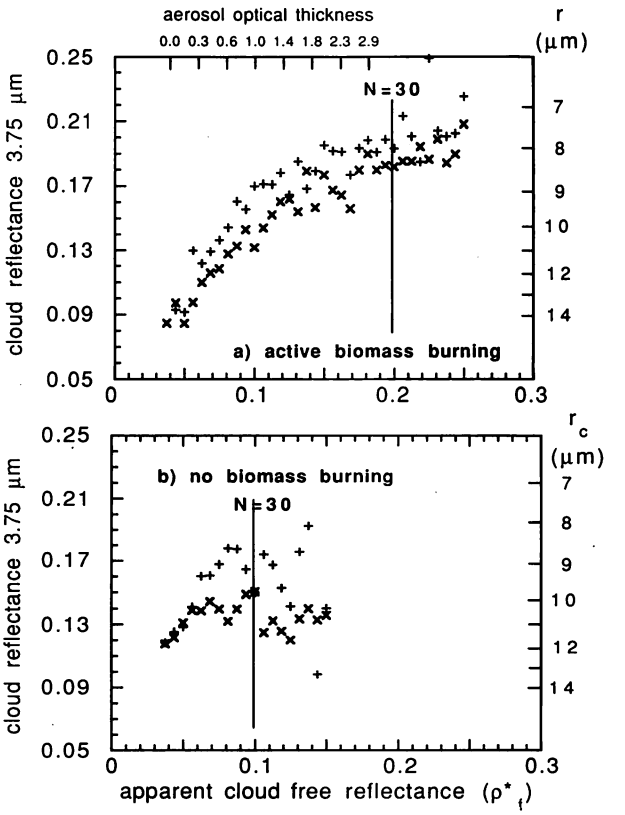

FIG. 6. Cloud reflectance at 3.75 μm as a function of the apparent cloud-free reflectance ρ_f^* at 0.64 μm, for period of time with (a) active biomass burning and smoke and for (b) a period preceding extensive biomass burning. The data are averaged for clouds observed in the near nadir direction ($\theta \leq 20°$) for the solar (×) and antisolar (+) directions. Cloud reflectance is averaged for bins of 0.005 in ρ_f^*. The number of clouds averaged for each data point is given in Fig. 5. The axes are also labeled by the corresponding drop radius r_c and by the smoke aerosol optical thickness for (a) only. The data to the left of the $N = 30$ lines are for more than 30 clouds in each average. Model simulations are shown by curve lines for four values of the imaginary part of the refractive index m_i.

The effect of smoke on cloud reflectivity in the 3.75-μm channel is compared in Fig. 6 for two datasets: a dataset taken in the fire season when smoke is likely to be present (Fig. 6a), and a dataset is taken from the beginning of the dry season when fires have not started yet (Fig. 6b). Cloud reflectance at 3.75 μm is plotted as a function of the apparent cloud-free reflectance at 0.64 μm, ρ_f^*. The radiance is derived from the AVHRR counts using inflight calibration (Holben et al. 1990). This apparent reflectance originates from reflection of sunlight from the earth's surface, scattering by smoke and other aerosols and molecules in the atmosphere. Here ρ_f^* is converted to the smoke optical thickness, assuming that the aerosol refractive index is $1.43–0.02i$. The imaginary part of the refractive index was adjusted to give a single-scattering albedo of 0.88, which is consistent with 6% graphitic carbon out of the total dry aerosol mass measured in Brazil (Andreae et al. 1988;

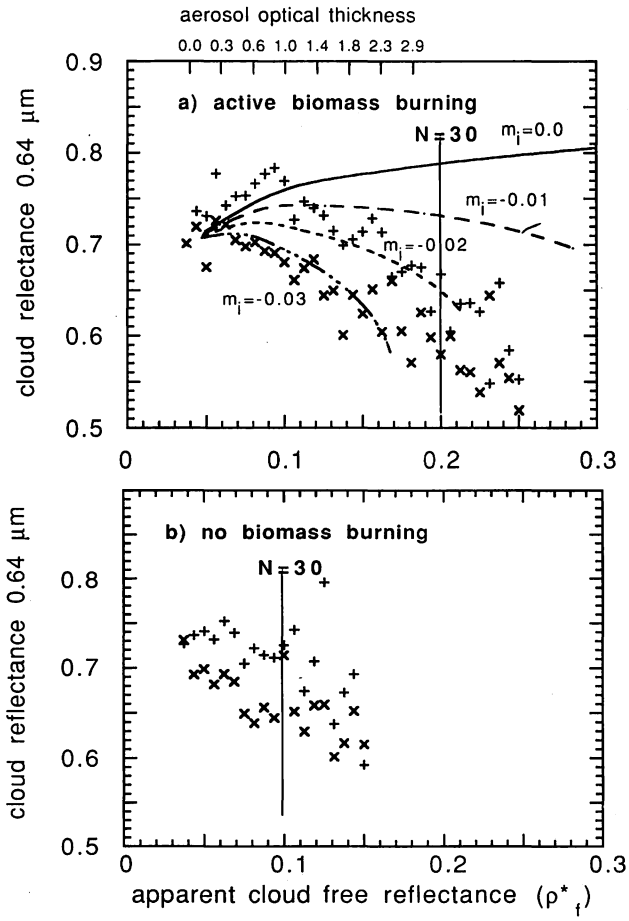

FIG. 7. Same as Fig. 6 but for the 0.64-μm AVHRR channel. Model simulations are shown by lines for four values of the imaginary part of the refractive index of the smoke.

Ward et al. 1991, 1992). The aerosol scattering properties were computed for a lognormal mass distribution with mean mass particle radius of 0.15 μm and standard deviation of $\ln r = 0.6$ (Kaufman et al. 1992). The surface reflectance is derived from the maximum of the histogram of the apparent cloud-free reflectances of images taken when biomass burning is not present (Fig. 6b). The surface reflectance that corresponds to the maximum in the smoke-free histogram, computed for a nominal background aerosol optical thickness $\tau_a = 0.1$, is 0.02.

The increase in the 3.75-μm reflectance as a function of the aerosol optical thickness (Fig. 6a) indicates the effect of smoke on reducing the cloud-drop size. Figure 6b shows that without smoke, cloud reflectance at 3.75 μm is much less dependent on ρ_f^*. Thus, as expected, the cloud drops become smaller mainly in the presence of smoke. The number of clouds used in the calculations of each point in Fig. 6, N, is larger than 30 to the left of the $N = 30$ line. The larger cloud statistics for $N > 30$ decreases the variation (Δ) in the reflectance in the 3.75-μm channel to less than $\Delta\rho_{3.7} = \pm 0.02$.

A comparison is made between the cloud reflectance in the 0.64-μm channel, $\rho_{0.64}$, for the dataset taken in the fire season (Fig. 7a) and the dataset from the beginning of the dry season, when fires have not started yet (Fig. 7b). The reflectance data were adjusted for the deterioration in the AVHRR sensor calibration of 20% (Holben et al. 1990). The data to the left of the $N = 30$ line have statistical noise $\Delta\rho_{0.64} = \pm 0.02$. The differences between the cloud characteristics during the fire season (Fig. 7a) and before the fire season (Fig. 7b) are not large but are important. In Fig. 7a, the cloud reflectance is nearly constant for $\rho_f^* < 0.08$ for the forward direction (×). In the backward direction (+), the reflectance increases initially and then decreases. This is due to the competing effects of cloud brightening due to an increase in the CCN concentration and cloud darkening due to absorption by graphitic carbon (Twomey 1977). The data are compared with theoretical analysis described in section 5.

Even though the analysis in Figs. 5–7 excludes the cloud perimeter, it is not assured that the smaller drop size present in the cloud edges (Coakley 1991) does not affect the results. Therefore, a similar analysis to the one shown in Figs. 6 and 7 was also performed using the properties of the brightest pixel in each cloud instead of the average of the nonperimeter pixels (Fig. 8). The brightest pixel of the cloud is usually located in the area of strongest convective activity far from the cloud edge, as indicated by its lower temperature. The results are very similar to those of average cloud properties shown in Figs. 6a and 7a. The decrease in the cloud reflectance in the 0.64-μm channel as a function of the smoke optical thickness is slightly smaller for the brightest pixels and the increase in the reflectance in the 3.75-μm channel is slightly larger. The variability in the data is larger since only one pixel from each cloud is used in the averaging process. Since the brightest pixel in each cloud is less affected by processes that take place at the cloud edges and generate a similar relationship as in Figs. 6 and 7, this analysis verifies that the results presented in Figs. 5 and 6 are not caused by the effect of cloud edges associated with broken cloud fields.

d. Other factors that may affect cloud properties

The variations in the cloud properties, shown in Figs. 6 and 7 were attributed to variations in the smoke optical thickness. It is important to verify that this change in the cloud properties is not a result of variation of other factors (e.g., variation in solar zenith angle). Therefore, the relationship between the variation in other measures for the same clouds and the variation in ρ_f^* is investigated. Table 2 summarizes the variations in these measures. There are small variations in some of the properties associated with the cloud field as the cloud-free reflectance increases from low $\rho_f^* = 0.05$ to 0.06 to high $\rho_f^* = 0.13$ to 0.17 values.

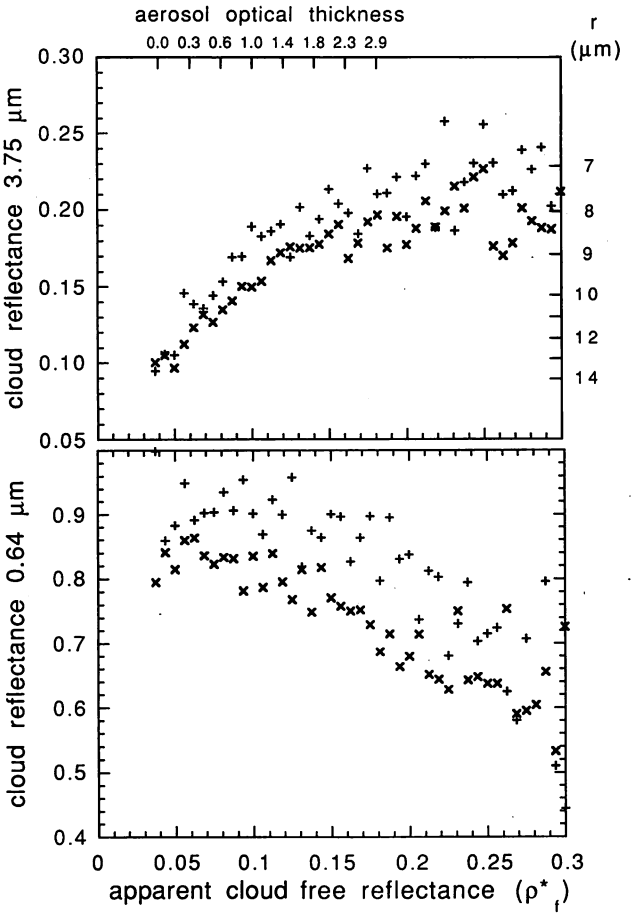

FIG. 8. Reflectance of the brightest pixel in each cloud at (a) 0.64 μm and (b) of same pixels at 3.75 μm grouped as a function of the apparent cloud-free reflectance ρ_f^* for a period of time with active biomass burning and smoke as in Figs. 6a and 7a. The data are averaged for clouds observed in the near nadir direction ($\theta \leq 20°$) for the solar (×) and antisolar directions (+). Cloud reflectance is averaged for bins of 0.005 in ρ_f^*. The number of clouds averaged for each data point is given in Fig. 5.

• The average cloud-top temperature increases from 277 to 282 K. This higher cloud-top temperature may be the result of reduction of convection due to the reduction of solar irradiation by the smoke and a corresponding reduction of the surface temperature of up to several degrees (Robock 1991). According to the statistical data shown in Fig. 2 (including properties of polluted and unpolluted clouds), an increase in the cloud-top temperature in this range is statistically associated with an increase in $\rho_{3.75}$ by approximately 0.02 and a decrease in $\rho_{0.64}$ by 0.02, which may explain part of the decrease in $\rho_{0.64}$ shown in Table 2 but only a minor part of the increase in $\rho_{3.75}$. The increase in the cloud-top temperature may be also associated with the breakup of the cloud layer. Coakley (1991) showed that in such a case, the reflectance of clouds in the 3.75-μm channel is increased by $\Delta\rho_{3.75} = 0.01$ (for the afternoon NOAA pass) for the present range of view directions ($0 \pm 20°$). Though breakup of the cloud layer, if occurring, may be a major contributor to the increase in the 3.75-μm reflectance shown in Fig. 2 for all the Amazonian clouds, it can be only a minor factor in the strong increase in the 3.75-μm reflectance as a function of the smoke concentration shown in Fig. 6.

• Solar zenith angle increases by 2°. It is not expected that this change can have a substantial effect.

• There is no substantial change in the average view direction that may affect the cloud radiative properties.

• Cloud-top roughness of 1°–2° can be the cause of the difference in cloud reflectance between the forward and backward directions (Figs. 6 and 7), which cannot be explained with a plane-parallel cloud model. An increase of 1° in the cloud-top roughness (representing roughness of approximately 200 m) as a function of ρ_f^* may be the basis for the difference between the forward and backward cloud reflectances shown in Figs. 6 and 7.

• Cloud area S and cloud shape factor $p^2/4\pi S$, where p is the cloud perimeter, are calculated as the number of pixels on the perimeter plus 4 (the addition of four accounts for the minimal number of perimeter pixels with at least two external faces). Note that if p would have been the true length of the perimeter, the minimum value of the shape factor would be 1.0 (for a circle). The area and the shape factor are indications of the cloud type and the convection process that takes place in the cloud. There is a small increase in these two parameters as a function of the smoke optical thickness. It is not clear what is the impact of a change in the convective process associated with this change in the cloud structure. If the increase in the cloud size

TABLE 2. Variation in the cloud properties and other measures as a function of the apparent cloud-free reflectance ρ_f^* and the corresponding smoke aerosol optical thickness τ_a. The values are for the 1987 main dataset (A), for view direction less than or equal to 20°, cloud-top temperature greater than or equal to 270 K, and cloud area greater than or equal to 9 km^2.

ρ_f^*	0.05–0.06	0.13–0.17
τ_a	0.1	2.0
Cloud reflectance at 0.64 μm	0.70–0.72	0.64–0.72
Cloud reflectance at 3.75 μm	0.08–0.09	0.15–0.18
Cloud-drop size	14–15 μm	8–9 μm
Number density of clouds[a]	10–50	50–70
Cloud-top temperature	277 K	282 K
Solar zenith angle	54°–57°	56°–59°
View zenith angle	7°–9°	8°–12°
Cloud-top roughness[b]	0°–1°	1°–2°
Cloud area (km^2)	18–30	20–50
Cloud shape factor[c]	1.3–1.4	1.4–1.8

[a] Number of clouds for a given range of ρ_f^*: $\Delta\rho_f^* = 0.005$.

[b] Cloud-top roughness is defined as the average cloud-top temperature (excluding the perimeter) minus the temperature of the brightest pixel in the cloud.

[c] Cloud shape factor is defined as $p^2/(4\pi S)$, where p is the cloud perimeter and S is the cloud area.

and reduction in the cloud-top temperature are indications of reduction in the updraft velocity, the resultant clouds may have fewer drops and smaller liquid water.

From the discussion that accompanied Table 2, it is concluded that the variation in the cloud reflectance in the visible and the mid-IR parts of the spectrum and the corresponding change in the drop size are indeed functions of the smoke optical thickness and cannot be explained by other factors.

e. Comparison to other biomass burning seasons

The effect of smoke aerosol on cloud properties in the 1987 biomass burning season was summarized in the last few sections. It is interesting to check if these properties can also be found in other dry seasons. In Table 3, several other fire seasons are analyzed. Note that for each fire season, the period of time varied as well. The period of the year that corresponds to the dry season and the strength of the dry season varies from year to year. For example, in 1989, the dry season was relatively wet. The cloud fraction was larger than in the other years and the rate of biomass burning was smaller. As a result, the initial drop size is different and the effect of smoke is smaller. The five images analyzed for 1981 were taken later in the dry season and exhibit a greater cloud fraction and apparently less biomass burning. All the fire seasons show a decrease in the cloud-drop size with the increase in the smoke optical thickness, accompanied with a decrease in $\rho_{0.64}$. The decrease in the drop size is maximal in 1984. In the restricted dataset that was used for the statistics in Table 3, the number of clouds in 1984 was rather small, but similar results were obtained in the analysis of Fig. 2 where the view direction was not limited to ±20°. The much wetter and cloudier years (1981 and 1989) showed a smaller reduction in the drop size.

5. Theoretical analysis

In this section we shall test if the measured effect of smoke particles on the cloud properties is in concert with a theoretical model based on Twomey (1977). First, a short review of the mathematical formulation for the effect of aerosol particles on cloud properties is given.

The relationship between the cloud-drop concentration N_d and the CCN concentration N_c depends on the maximum supersaturation reached in the cloud, which depends in turn on the updraft speed. For 1% supersaturation, the relationship is described by Twomey (1959, 1977) and Twomey et al. (1984):

$$N_d \propto N_c^{2/(k+2)}, \tag{4}$$

where k was found empirically typically as $k \sim 0.5$ (Twomey 1977). Braham (1974) measured N_d and N_c for continental air. The value of k that fits his measurements is $k = 0.8 \pm 0.15$ (Kaufman et al. 1991). Note that for higher values of k, the cloud-drop concentration N_d is less dependent on variations of the CCN concentration caused by an increase in pollution levels. The relationship between the cloud-drop concentration and the CCN takes into account the effect of CCN concentration on the maximum supersaturation and was used successfully to predict cloud-drop concentration (Twomey and Warner 1967).

The optical thickness of the cloud in the solar spectrum is computed using geometrical optics since the cloud-drop size is much larger than the wavelength. For a fixed amount of liquid water, the increase in the cloud-drop concentration from a background value of

TABLE 3. Variation in the average cloud properties and other measures, as in Table 2 but for 1981, 1984, and 1989. Low smoke is defined for $\rho_f^* = 0.05$ to 0.06 ($\tau_a = 0.1$) and heavy smoke for $\rho_f^* = 0.13$ to 0.15 ($\tau_a = 2.0$).

Year	1981		1984		1989	
Period	September–October		August–September		September	
Smoke load:	Low	Heavy	Low	Heavy	Low	Heavy
τ_a	0.1	2.0	0.1	2.0	0.1	2.0
Cloud reflectance						
at 0.64 μm	0.66–0.75	0.56–0.65	0.62–0.71	0.56–0.66	0.65–0.72	0.59–0.72
at 3.75 μm	0.08–0.10	0.12–0.15	0.04–0.05	0.14–0.23	0.11–0.16	0.16–0.20
Cloud-drop size (μm)	13–15	10–11	20–23	7–10	9–12	8–9
Number of clouds[a]	10–40	10–40	1–10	1–10	10–30	10–30
Cloud-top temperature	278 K	280 K	276 K	280 K	278 K	277 K
Solar zenith angle	41°–43°	41°–43°	57°–59°	59°–64°	31°–34°	32°–36°
Cloud-top roughness[b]	0°–1°	0°–1.5°	0°–1°	0°–3°	0.5°	0.5°–1.5°
Cloud area km^2	17–19	30–60	10–18	20–100	16–18	15–40
Cloud shape factor[c]	1.3–1.4	1.9–2.4	1.4–1.5	1.6–2.0	1.4–1.5	1.4–1.7

[a] Number of clouds for a given range of ρ_f^*: $\Delta\rho_f^* = 0.005$.

[b] Cloud-top roughness is defined as the average cloud-top temperature (excluding the perimeter) minus the temperature of the brightest pixel in the cloud.

[c] Cloud shape factor is defined as $p^2/(4\pi S)$, where p is the cloud perimeter and S is the cloud area.

N_{do} to N_d, causes a decrease in the drop size from r_{co} to r_c and an increase in the cloud optical thickness (Twomey et al. 1984) from τ_{co} to τ_c:

$$\frac{\tau_c}{\tau_{co}} = \left(\frac{N_d}{N_{do}}\right)^{1/3} = \frac{r_{co}}{r_c}. \quad (5)$$

An increase in the smoke aerosol optical thickness is expected to increase the CCN concentration and the cloud-drop concentration and to change the drop size and cloud optical thickness via the relationship given in (5). No attempt will be made here to formulate the relationship between the aerosol optical thickness and the cloud-drop concentration since it depends on several uncertain factors that cannot be measured from space (Kaufman et al. 1990a), such as:

- the relationship between the smoke optical thickness and the aerosol volume concentration;
- the fraction of the aerosol particles activated in the cloud—this fraction depends on the particles size distribution and on the maximum supersaturation reached in the cloud, both of which may vary as a function of the aerosol optical thickness;
- the drop concentration in the unperturbed clouds.

As a result, measured relationship between the cloud reflectance at 3.75 μm and the smoke optical thickness is used to derive the relationship between the drop size and the smoke optical thickness. The variation in the cloud optical thickness is subsequently derived from (5) and a radiative transfer model is used to compute the variation in the cloud reflectance at 0.64 μm. The dependence of this reflectance on the smoke optical thickness is then compared to the measured one. The following will describe the comparison.

The determination of τ_{co} and r_{co} is based on the measurements of the cloud reflectance in the 0.64-μm and 3.75-μm channels for values of ρ_f^* that correspond to the smoke-free conditions ($\rho_f^* = 0.04 - 0.05$ in Figs. 6 and 7). The radiative code of Nakajima and Tanaka (1986, 1988) is used in the theoretical computations in this paper. The resultant values are $\tau_{co} = 50$ and $r_{co} = 14.4$ μm. In the computations, Mie theory was used for homogeneous spheres to compute the optical properties of the cloud drops. The effective cloud absorption in the 0.64-μm channel was artificially doubled in order to account for the higher absorption by cloud drops with impurities of graphitic carbon rather than a homogeneous medium (Twohy et al. 1989). It is also assumed that 30% of the smoke particles interact with the cloud and 70% stay beneath the cloud base.

An analytical approximation is used for the relationship between the cloud reflectance in the 3.75-μm channel and the drop size. For moderate to thick clouds ($\tau_c > 8$), this relationship is almost independent of other cloud properties, for example, cloud optical thickness, temperature, presence of graphitic carbon, or the cause for the given drop size. Figure 9 shows the results of radiative transfer computations (symbols) of the relationship between the reflectance in the 3.75-μm channel and the drop size for several values of the smoke optical thickness. It also shows an empirical approximation (solid line) for this relationship:

$$\ln\rho_{3.7} = -0.6846 - 0.08243r_c - 0.00749r_c^2 + 0.00033r_c^3 \quad (6)$$

in Fig. 9. The remotely sensed relationship between the cloud reflectance at 3.75 μm, $\rho_{3.7}$, and the apparent cloud-free reflectance, ρ_f^* at 0.64 μm, shown in Fig. 6a can be approximated by:

$$\ln\rho_{3.7} = -\frac{0.0427}{\rho_f^*} - 1.44. \quad (7)$$

The average of the solar and antisolar measured cloud reflectances, $\rho_{3.7}$, and the optimum fit to the measured reflectances is shown in Fig. 10a as a function of the cloud-free reflectance (ρ_f^*). Combination of (6) and (7) gives the empirical relation between the smoke effect on the apparent cloud-free reflectance and the cloud-drop size. This relation is used to compute the model prediction for the variation in the cloud reflectance at 0.64 μm as a function of the smoke concentration for a fixed amount of liquid water. Note that the increase in the cloud-top temperature, with the increase in the smoke concentration (shown in Table 2), indicates a possible reduction of the liquid water content. For smaller liquid water content, the cloud optical

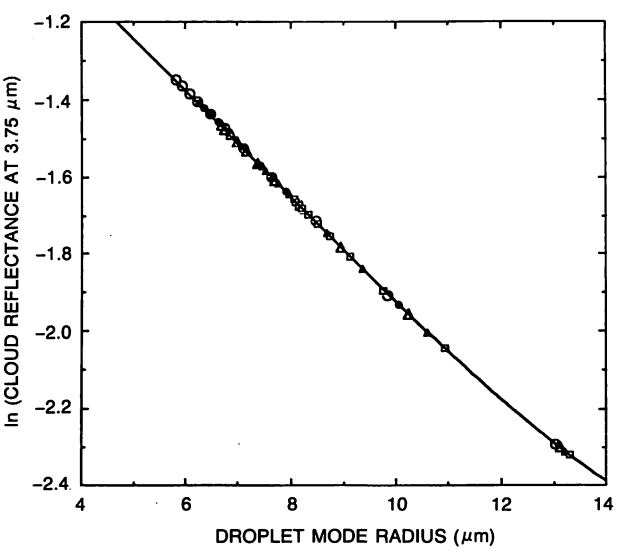

FIG. 9. Relation between the cloud reflectance in the 3.75-μm channel and the drop size computed using the radiative transfer code of Nakajima and Tanaka (1986 and 1988) for cloud optical thickness in the visible part of the spectrum above 50. The different symbols represent several values of the smoke aerosol imaginary index used in the computations. The relation is fitted by $\ln(\rho_{3.7}) = a_0 + a_1r_c + a_2r_c^2 + a_3r_c^3$ [Eq. (6)].

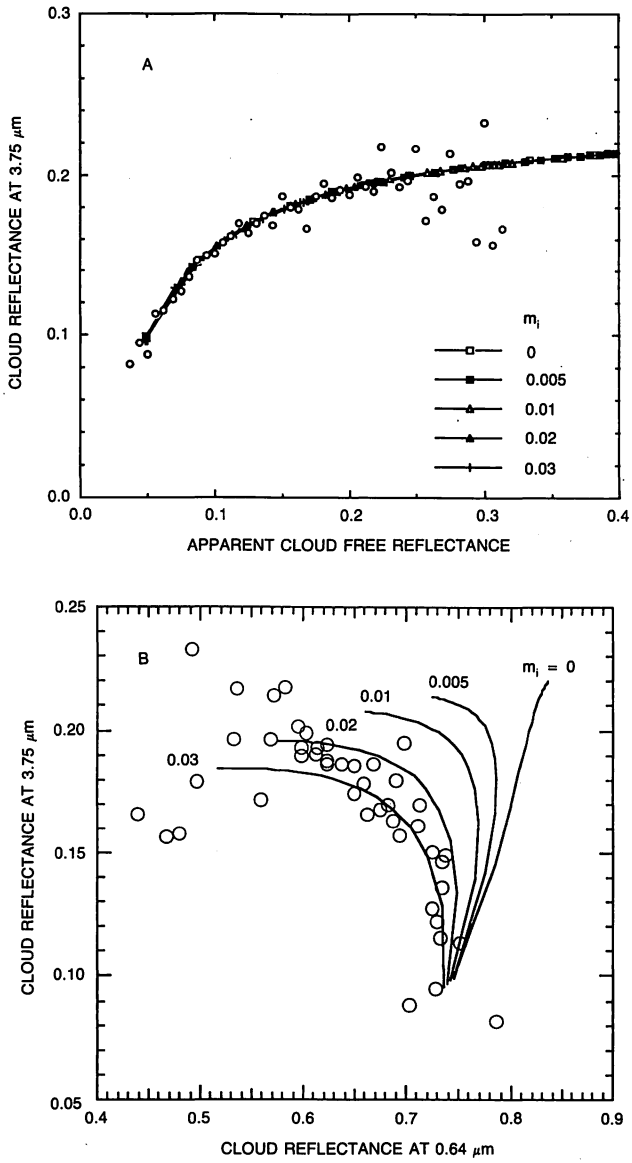

FIG. 10. (a) Best fit to the relation between the cloud reflectance in the 3.75-μm channel and the apparent cloud-free reflectance representing the smoke density. The AVHRR measurements are averaged for equal steps of the cloud-free apparent reflectance ρ_f^* and the theoretical values are computed for five values of the imaginary part of the refractive index. An analytical expression [Eq. (7)] is used to fit the theoretical computations. (b) Scatter diagram of the cloud reflectance in the 3.75-μm channel and the cloud reflectance in the 0.64-μm channel. The AVHRR cloud data are averaged for equal steps of ρ_f^*. Theoretical computations based on the relation between the cloud-drop size and the cloud-free apparent reflectance are shown for five values of the imaginary index of the smoke particles.

thickness would have been smaller than indicated by (5) and the corresponding cloud reflectance at 0.64 μm would be smaller as well. Due to the lack of appropriate measures, no attempt is made to account for this possibility in the theoretical evaluation. The results are shown in Fig. 7a for several values of the aerosol imaginary index. A scatter diagram of the measured cloud reflectance in the 3.75-μm channel as a function of the cloud reflectance in the 0.64-μm channel is shown in Fig. 10b. Both comparisons (Figs. 7a and 10b) show a very good fit for m_i between 0.02 and 0.03. Note that the range of the values of the imaginary index (0.02–0.03) agrees with the average single-scattering albedo ω_0 measured by Radke et al. (1991) for fires in North America ($\omega_0 = 0.83$) and ω_0 computed for the measured amount of graphitic carbon in the Amazon Basin (Holben et al. 1991; $\omega_0 = 0.88$).

The measured cloud reflectances in the 0.64-μm and 3.75-μm channels are also plotted versus each other in Fig. 1. Note that the data indicate a reduction of the reflectance in the 0.64-μm channel with a decrease of the cloud-drop size. This reduction in the reflectance is interpreted in the figure as a reduction of the optical thickness, since the theoretical contour lines were computed for a constant absorption in the cloud. In reality, the cloud optical thickness probably increases with the reduction in the drop size [according to (5)] and reduction in the cloud reflectance results from an increase in the amount of graphitic carbon in the cloud due to the increase of the smoke optical thickness.

6. Conclusions

The effect of aerosol concentration on cloud microphysics and cloud albedo is tested by examining smoke aerosol and clouds in the tropics; AVHRR images from the dry season in Brazil are used for this purpose. A detailed analysis of images from 1987 taken before and during active biomass burning shows that an increase in the smoke concentration, manifested by increase in the smoke optical thickness derived from the cloud-free reflectance, resulted in clouds that have a smaller drop size and that are darker in the visible part of the spectrum. From satellite data, it is impossible to derive all the parameters that influence cloud properties and smoke–cloud interaction. Satellite data can, however, be used to generate large-scale statistics of the properties of clouds and surrounding aerosol (e.g., smoke optical thickness, cloud-drop size, and cloud reflection of solar radiation) from which the interaction of aerosol with clouds can be surmised. Images from three other years were also analyzed for comparison. The average drop size decreased by 6 μm from 15 to 9 μm in 1987. It decreased more during a dry year (more smoke, by 13 μm in 1984) than during a wet year (less smoke, 2 μm in 1989). The average cloud reflectance in the visible part of the spectrum decreased by $\Delta\rho_c = 0.03$ from the average smoke-free value of $\rho_c = 0.7$ in 1987, most likely due to the effect of graphitic carbon absorption on the reflectance of the bright clouds. The increase in the average cloud-top temperature as a function of the smoke optical thickness indicates the possibility that reduction of convection due to the smoke absorption and reflection of sunlight caused a decrease in the up-

draft speed and in the amount of liquid water available to form the cloud. Note that fires generate strong convection resulting in high and reflective clouds. Reduction of the cloud liquid water can contribute to reduction in its reflectivity at 0.64 μm through a reduction in cloud-drop density. The observed increase in the cloud reflectivity at 3.75 μm as a function of the smoke optical thickness was inverted into the cloud-drop size and used to predict, based on Twomey's theory, the change in the cloud reflectivity at 0.64 μm. The results were found to fit very reasonably to the measured reflectivity of the cloud. The theoretical computations are based on the assumption that the cloud liquid water is kept constant; therefore, the present study indicates that reductions in the cloud liquid water cannot have a dominant effect on the cloud properties. Though the present analysis may have missed smaller, less developed, clouds (with reflectance smaller than 0.4), the results indicate that smoke reduces rather than increases the reflectivity of clouds in the tropics, in contrast to previous assumptions (Penner et al. 1991) but in agreement with Twomey's theory (Twomey 1977). Smoke aerosol particles have similar properties (e.g., size distribution) to maritime and anthropogenic aerosol and therefore, in general, can represent the effect on bright clouds by anthropogenic aerosol. The effect of the aerosol particles on cloud microphysics depends to a large extent on the details of the size distribution for small particle radius (<0.1 μm); these particles can form high CCN concentrations without representing a large fraction of the aerosol mass. The exact shape of the size distribution of the smoke, or of maritime and anthropogenic particles, depends on the distribution of sources and the age of the aerosol layer. Therefore, the magnitude of the effect of smoke on clouds may differ from the effect of anthropogenic or maritime particles. In order to better understand the interaction of aerosol particles with clouds, more information about the details of their size distribution and time evolution are required.

Acknowledgments. We would like to thank Robert Fraser and Albert Arking from NASA/GSFC, Mark Lawrence from Georgia Tech/USRA Visiting Scientist Program, and Lorraine Remer from SSAI for critical review and helpful discussion during this work, Shana Mattoo from ARC for the analysis of the AVHRR images, and J. Tucker from NASA/GSFC for collecting and providing us with this unique AVHRR dataset.

REFERENCES

Albrecht, B. A., 1989: Aerosol cloud microphysics and fractional cloudiness. *Science,* **245,** 1227–1230.

Andreae, M. O., E. V. Browell, M. Garstang, G. L. Gregory, R. C. Harris, G. F. Hill, D. J. Jaqcob, M. C. Pereira, G. W. Sachse, A. W. Setzer, P. L. Silva Dias, R. W. Tablot, A. L. Torres, and S. C. Wofsy, 1988: Biomass burning emissions and associated haze layers over Amazonia. *J. Geophys. Res.,* **93,** 1509–1527.

Arking, A., and J. D. Childs, 1985: Retrieval of cloud cover parameters from multispectral satellite images. *J. Climate Appl. Meteor.,* **24,** 322–333.

Baker, M. B., and R. J. Charlson, 1990: Bistability of CCN concentrations and thermodynamics in the cloud-topped boundary layer. *Nature,* **345,** 142–145.

Braham, R. R., Jr., 1974: Cloud physics of urban weather modification—A preliminary report. *Bull. Amer. Meteor. Soc.,* **55,** 100–106.

Charlson, R. J., J. Langer, and H. Rodhe, 1990: Sulphate aerosol and climate. *Nature,* **348,** 22.

——, ——, H. Rodhe, C. B. Leovy, and S. G. Warren, 1991: Perturbation of the Northern Hemispheric radiative balance by backscattering from anthropogenic sulfate aerosol. *Tellus,* **43AB,** 152–163.

Coakley, J. A., Jr., 1991: Reflectivities of uniform and broken layered clouds. *Tellus,* **43B,** 420–433.

——, and F. P. Bretherton, 1982: Cloud cover from high resolution scanner data: Detecting and allowing for partially filled fields of view. *J. Geophys. Res.,* **87,** 4917–4932.

——, R. D. Cess, and F. B. Yurevich, 1983: The effect of tropospheric aerosol on the earth's radiation budget: A parametrization for climate models. *J. Atmos. Sci.,* **40,** 116–138.

——, R. L. Bernstein, and P. A. Durkee, 1987: Effect of ship stack effluents on cloud reflectance. *Science,* **237,** 953–1084.

Crutzen, P. J., and M. O. Andreae, 1990: Biomass burning in the tropics: Impact on atmospheric chemistry and biogeochemical cycles. *Science,* **250,** 1669–1678.

——, A. C. Delany, J. Greenberg, P. Haggenson, L. Heidt, R. Lueb, W. Pollock, W. Seiler, A. Wartburg, and P. Simmerman, 1985: Tropospheric chemical composition measurements in Brazil during the dry season. *J. Atmos. Chem.,* **2,** 233–256.

Fraser, R. S., Y. J. Kaufman, and R. L. Mahoney, 1984: Satellite measurements of aerosol mass and transport. *Atmos. Environ.,* **18,** 2577–2584.

Hansen, J., and A. A. Lacis, 1990: Sun and dust versus greenhouse gases: An assessment of their relative roles in global climate change. *Nature,* **346,** 713–719.

——, ——, D. Rind, G. Russel, P. Stone, I. Fung, R. Ruedy, and J. Lerner, 1984: Climate sensitivity: Analysis of feedback mechanisms. *Climate Processes and Climatic Sensitivity,* J. E. Hansen and T. Takahashi, Eds., Amer. Geophys. Union, 130–163.

Hobbs, P. V., and L. F. Radke, 1969: Cloud condensation nuclei from a simulated forest fire. *Science,* **163,** 279–280.

——, ——, and S. E. Shumway, 1970: Cloud condensation nuclei from industrial sources and their apparent influence on precipitation in Washington state. *J. Atmos. Sci.,* **27,** 81–89.

Holben, B. N., Y. J. Kaufman, and J. D. Kendall, 1990: NOAA-11 AVHRR visible and near-IR inflight calibration bands. *Int. J. Rem. Sens.,* **11,** 1511–1519.

——, ——, D. Tanré, and D. E. Ward, 1991: Optical properties of aerosol from biomass burning in the tropics. *BASE-A Global Biomass Burning,* The MIT press, 403–411.

Isaac, G. A., W. R. Leaitch, J. W. Strapp, and K. G. Anlauf, 1986: Summer aerosol profiles over Algonquin Park, Canada. *Atmos. Environ.,* **24A,** 3033–3046.

Kaufman, Y. J., 1989: The atmospheric effect on remote sensing and its correction. *Optical Remote Sensing, Technology and Application.* G. Asrar, Ed., Wiley.

——, and C. Sendra, 1988: Algorithm for atmospheric corrections of visible and near IR satellite imagery. *Int. J. Remote. Sens.,* **9,** 1357–1381.

——, R. S. Fraser, and R. A. Ferrare, 1990a: Satellite remote sensing of large scale air pollution—Method. *J. Geophys. Res.,* **95,** 9895–9909.

——, C. J. Tucker, and I. Fung, 1990b: Remote sensing of biomass burning in the tropics. *J. Geophys. Res.,* **95,** 9927–9939.

——, ——, and R. L. Mahoney, 1991: Fossil fuel and biomass burning effect on climate—Heating or cooling? *J. Climate,* **4,** 578–588.

——, A. Setzer, D. Ward, D. Tanré, B. N. Holben, P. Menzel, M. C. Pereira, and R. Rasmussen, 1992: Biomass Burning Air-

borne and Spaceborne Experiment in the Amazonas (BASE-A). *J. Geophys. Res.*

King, M. D., and Harshvardhan, 1986: Comparative accuracy of the albedo, transmission and absorption for selected radiative transfer approximations. NASA Reference Publication, **1160,** 41 pp.

Leaitch, W. R., J. W. Strapp, and G. A. Issac, 1986: Cloud droplet nucleation and cloud scavenging of aerosol sulphate in polluted atmospheres. *Tellus,* **38B,** 328–344.

——, G. A. Isaac, J. W. Strapp, C. M. Banic, and H. A. Wiebe, 1992: The relationship between cloud droplet number concentrations and anthropogenic pollution: Observations and climatic implications. *J. Geophys. Res.,* **97,** 2463–2474.

Malingreau, J., and C. J. Tucker, 1988: Large scale deforestation in the Southeastern Amazon Basin of Brazil. *Ambio,* **17,** 49–55.

Manabe, S., and R. T. Wetherald, 1980: On the distribution of climate change resulting from an increase in the CO_2 content of the atmosphere. *J. Atmos. Sci.,* **37,** 99–118.

Nakajima, T., and M. Tanaka, 1986: Matrix formulations for the transfer of solar radiation in a plane-parallel scattering atmosphere. *J. Quant. Spectrosc. Rad. Transfer,* **35,** 13–21.

——, and ——, 1988: Algorithms for radiative intensity calculations in moderately thick atmospheres using a truncation approximation. *J. Quant. Spectrosc. Rad. Transfer,* **40,** 51–69.

——, and M. D. King, 1990: Determination of the optical thickness and effective particle radius of clouds from reflected solar radiation measurements. Part I: Theory. *J. Atmos. Sci.,* **47,** 1878–1893.

——, ——, J. D. Spinhirne, and L. F. Radke, 1991: Determination of the optical thickness and effective particle radius of clouds from reflected solar radiation measurements. Part II: Marine stratocumulus observations. *J. Atmos. Sci.,* **48,** 728–750.

Penner, J. E., R. E. Dickinson, C. A. O'Neill, 1992: Effects of aerosol from biomass burning on the global radiation budget. *Science,* **256,** 1432–1434.

——, S. J. Ghan, and J. J. Walton, 1991: The role of biomass burning in the budget and cycle of carbonaceous soot aerosol and their climatic impact. *Global Biomass Burning,* The MIT Press, 387–393.

Peterson, J. T., E. C. Flowers, G. J. Berri, C. L. Reynolds, and J. H. Rudisil, 1981: Atmospheric turbidity over central North Carolina. *J. Appl. Meteor.,* **20,** 229–241.

Radke, L. F., 1989: Airborne observations of cloud microphysics modified by anthropogenic forcing. *Symp. on Atmospheric Chemistry and Global Climate,* Anaheim, Amer. Meteor. Soc., 310–315.

——, J. A. Coakley, Jr., and M. D. King, 1989: Direct and remote sensing observations of the effect of ships on clouds. *Science,* **246,** 1146–1149.

——, D. A. Hegg, P. V. Hobbs, J. D. Nance, J. H. Lyons, K. K. Laursen, P. J. Reagan, and D. E. Ward, 1991: Particulate and trace gas emission from large biomass fires in North America. *Global Biomass Burning,* The MIT Press, 209–224.

Rawlins, F., and J. S. Foot, 1990: Remotely sensed measurements of stratocumulus properties during FIRE using the C130 aircraft multichannel radiometer. *J. Atmos. Sci.,* **47,** 2488–2503.

Setzer, A. W., and M. C. Pereira, 1991: Amazonia biomass burnings in 1987 and an estimate of their tropospheric emissions. *Ambio,* **20,** 19–22.

Squires, P., 1956: The microstructure of cumuli in maritime and continental air. *Tellus,* **8,** 443.

——, 1966: An estimate on the anthropogenic production of cloud nuclei. *J. Rech. Atmos.,* **2,** 297–308.

——, and S. Twomey, 1960: The relation between cloud droplet spectra and the spectrum of cloud nuclei. Physics of Precipitation, *Amer. Geophys. Union, Geophys. Monograph,* **5,** 211–219.

Stith, J. L., L. F. Radke, and P. V. Hobbs, 1981: Particle emission and the production of ozone and nitrogen oxides from the burning of forest slash. *Atmos. Environ.,* **15,** 73–82.

Stephens, G. L., and S.-C. Tsay, 1990: On the cloud absorption anomaly. *Quart. J. Roy. Meteor. Soc.,* **116,** 671–704.

Tucker, C. J., B. N. Holben, and T. E. Goff, 1984: Intensive forest clearing in Rondonia, Brazil, as detected by satellite remote sensing. *Rem. Sens. Environ.,* **15,** 255.

Twohy, C. H., A. D. Clarke, S. G. Warren, L. F. Radke, and R. J. Charlson, 1989: Light absorbing material extracted from cloud droplets and its effect on cloud albedo. *J. Geoph. Res.,* **94,** 8623–8631.

Twomey, S. A., 1959: The nuclei of natural cloud formation II. *Geofis. Pura Appl.,* **43,** 243–249.

——, 1977: The influence of pollution on the short wave albedo of clouds. *J. Atmos. Sci.,* **34,** 1149–1152.

——, 1991: Aerosols, clouds and radiation. *Atmos. Environ.,* **25a,** 2435–2442.

——, and J. Warner, 1967: Comparison of measurements of cloud droplets and cloud nuclei. *J. Atmos. Sci.,* **24,** 702–703.

——, and T. A. Wojciechowski, 1969: Observations of the geographical variation of cloud nuclei. *J. Atmos. Sci.,* **26,** 684–688.

——, and T. Cocks, 1982: Spectral reflectance of clouds in the near IR: Comparison of measurements and calculations. *J. Meteor. Soc. Japan,* **60,** 583–592.

——, and ——, 1989: Remote sensing of cloud parameters from spectral reflectance in the near IR. *Contr. Atmos. Phys.,* **62,** 172–179.

——, M. Piepgrass, and T. L. Wolfe, 1984: An assessment of the impact of pollution on the global albedo. *Tellus,* **36B,** 356–366.

Ward, D. E., A. Setzer, Y. Kaufman, and R. Rasmussen, 1991: Characteristics of smoke emissions from biomass fires of the Amazon region—BASE-A experiment. *Global Biomass Burning,* The MIT Press, 394–402.

——, R. Susott, J. Kauffman, R. Babbitt, B. N. Holben, Y. J. Kaufman, A. Setzer, R. Rasmussen, D. Cumming, and B. Dias, 1992: Emissions and burning characteristics of biomass fires for cerrado and tropical forest regions of Brazil—BASE-B experiment. *J. Geophys. Res.*

Warner, J., 1968: A reduction in rainfall associated with smoke from sugar-cane fires—An inadvertent weather modification? *J. Appl. Meteor.,* **7,** 247–251.

——, and S. Twomey, 1967: The production of cloud nuclei by cane fires and the effect on cloud droplet concentration. *J. Atmos. Sci.,* **24,** 704–706.

Wigley, T. M. L., 1989: Possible climate change due to SO_2 derived cloud condensation nuclei. *Nature,* **339,** 355–357.

——, 1991: Could reducing fossil-fuel emissions cause global warming? *Nature,* **349,** 503–506.